

# Fabrication of Ultrathin 2D Cu-BDC Nanosheets and the Derived Integrated MOF Nanocomposites

Guowu Zhan,\* Longlong Fan, Feigang Zhao, Zhongliang Huang, Bin Chen, Xin Yang, and Shu-feng Zhou

Freestanding 2D nanosheets with many unprecedented properties have been used in a myriad of applications. In this work, 2D copper-bearing metal-organic frameworks (MOFs; viz., Cu-BDC) nanosheets are successfully fabricated via a facile and benign methodology through using Cu<sub>2</sub>O nanocubes (≈60 nm) as a confined metal ion source and 1,4-benzenedicarboxylic acid (H<sub>2</sub>BDC) as an organic linker. The Cu<sub>2</sub>O nanocubes gradually release Cu<sup>+</sup> ions which are further oxidized by the dissolved oxygen and serve as nutrients for construction of 2D frameworks. In contrast, the conventional solvothermal synthesis with copper salt exclusively yields bulk Cu-BDC with edge dimensions of 2–10 μm. Interestingly, the as-prepared Cu-BDC nanosheets show ultrathin thickness, oriented growth, and excellent crystallinity, which can be exploited as a platform for the design of a series of 2D-integrated nanocatalysts by loading various metal nanocrystals such as Au, Ag, Pt, and Ru, with 3-mercaptopropionic acid as molecular link. In addition, it is found that Cu-BDC/M composites with highly accessible active sites on the surface exhibit high catalytic activity in several condensation reactions between benzaldehyde and primary amines. The findings offer an alternative strategy for rational design and synthesis of 2D MOF nanosheets and the derived 2D nanocomposites for catalytic applications.

## 1. Introduction

Metal-organic frameworks (MOFs) with networks of metal ions coordinated to multidentate organic molecules have been extensively studied in the past two decades.<sup>[1–4]</sup> According to provisional statistics, more than 20 000 different MOFs have been reported.<sup>[5]</sup> Different from the straightforward synthesis of MOFs by using well-soluble salts as metal ion source, some special examples have been recently reported to use Cu-based solid materials as metal ion source to produce Cu-bearing MOFs,<sup>[6–11]</sup> such as copper hydroxide, copper hydroxysulfate, copper electrode, cuprous oxide, or even copper net. It is

important to note that, differing from the traditional methods, copper ions from insoluble solid materials are gradually released, and then consumed as nutrients for MOF growth. However, most of the products were irregular in geometric shapes; therefore, it is a great challenge to control the shape of MOFs, particularly the 2D nanosheets.<sup>[12–14]</sup>

Cu-BDC (where BDC<sup>2-</sup> = 1,4-benzenedicarboxylate) as a typical copper-bearing MOFs has attracted many research interests in the past years.<sup>[15–20]</sup> As shown in Figure 1a–d, the building block unit in Cu-BDC framework contains two 5-coordinate copper cations bridged in a paddle-wheel-type configuration and to which the terephthalate ligands (BDC<sup>2-</sup>) are coordinated in a bidentate bridging fashion.<sup>[16]</sup> Besides the carboxylic ligands, one terminal dimethylformamide (DMF) is also coordinated with the copper ions.<sup>[21]</sup> Therefore, similar to HKUST-1, copper sites in Cu-BDC are ready to lose their reversibly coordinated DMF solvent upon thermal activation, which leads to open

coordination sites and thereby work well as heterogeneous Lewis acid catalysts towards a rich variety of reactions including aerobic homocoupling of arylboronic acids,<sup>[22]</sup> Friedlander reaction,<sup>[23]</sup> three-component couplings of amines, aldehydes, and alkynes,<sup>[24]</sup> acetylation of alcohols,<sup>[25]</sup> cyclization reaction,<sup>[26]</sup> direct oxidative C–C coupling,<sup>[27]</sup> and the like. Accordingly, Cu-BDC has received intense attention similar to the traditional Cu-based nanostructured materials in catalysis.<sup>[28]</sup> Considering that the crystal structure of Cu-BDC belongs to monoclinic, C2/m space group ( $a = 11.4 \text{ \AA}$ ,  $b = 14.3 \text{ \AA}$ ,  $c = 7.8 \text{ \AA}$ , and  $\beta = 108^\circ$ ),<sup>[16]</sup> the intrinsic structure anisotropy is possible for 2D growth of the MOFs. Therefore, herein, we present a new synthetic strategy for Cu-BDC nanosheets by using Cu<sub>2</sub>O nanocubes as a copper ion source at benign conditions.

However, although the pristine MOFs own some catalytic abilities,<sup>[29]</sup> the nanocomposites of MOFs and metal nanoparticles (MNPs) have emerged as sustainable alternatives to the conventional heterogeneous catalysts,<sup>[30–35]</sup> wherein MOFs serve as support materials or encapsulation shells.<sup>[13,36,37]</sup> For instance, microporous MOFs can provide a large surface area for loading MNPs working similarly to the mesoporous carbon and silica, where the interactions between the MNPs and the

Prof. G. Zhan, L. Fan, F. Zhao, Z. Huang, B. Chen, Dr. X. Yang, Prof. S.-f. Zhou  
College of Chemical Engineering  
Huaqiao University  
668 Jimei Boulevard, Xiamen, Fujian 361021, P. R. China  
E-mail: gwzhan@hqu.edu.cn

 The ORCID identification number(s) for the author(s) of this article can be found under <https://doi.org/10.1002/adfm.201806720>.

DOI: 10.1002/adfm.201806720

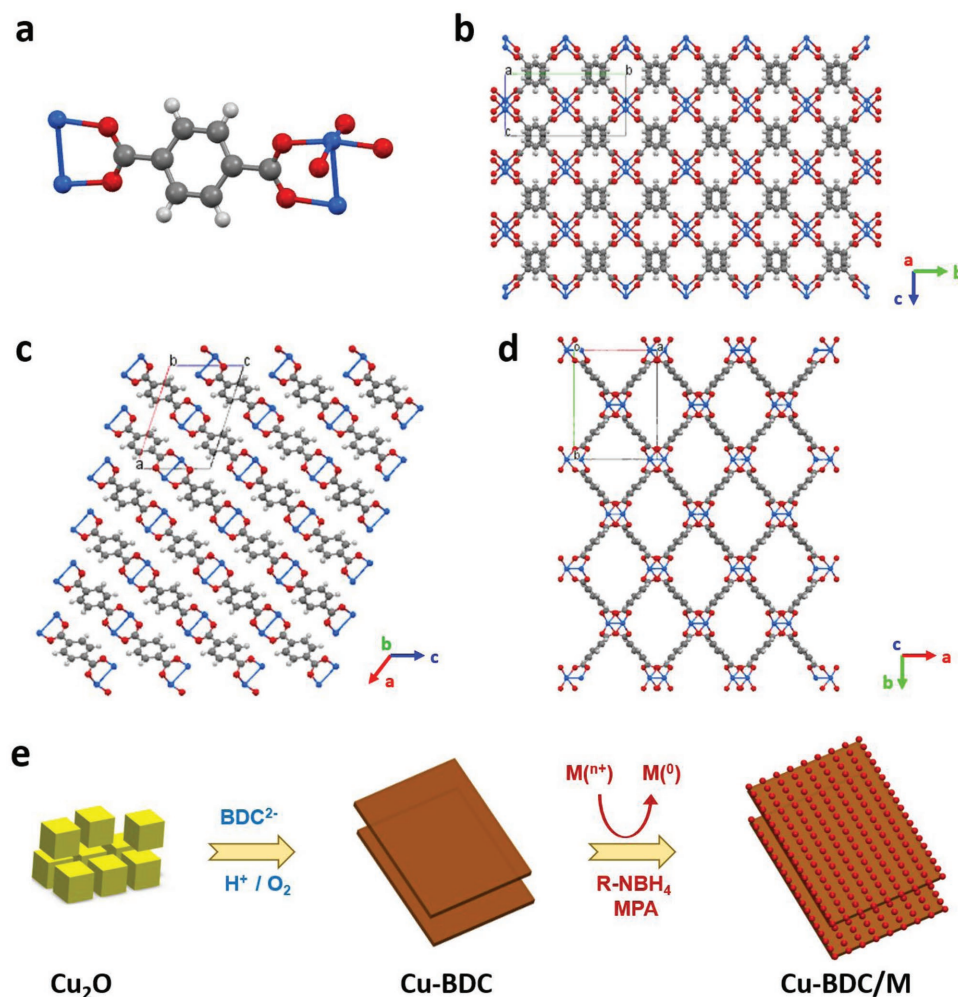


**Figure 1.** a) Dicopper(II) paddle-wheel building block for Cu-BDC frameworks. Copper, oxygen, carbon, and hydrogen atoms are shown in blue, red, gray, and white, respectively. Cu–Cu distance is 0.263 nm. b–d) Different views of a portion of the Cu-BDC structure, wherein guest molecules were omitted for clarity. The crystallographic data were obtained from The Cambridge Crystallographic Data Centre (CCDC-687690).<sup>[16]</sup> e) Schematic illustration of the synthesis of Cu-BDC nanosheets and the deviated nanocatalysts, starting from Cu<sub>2</sub>O nanocubes as raw materials. MPA = 3-mercaptopropionic acid, and R-NBH<sub>4</sub> = tetrabutylammonium borohydride.

MOFs are very important for preventing the agglomeration of the MNPs in catalysis applications. For MNP@MOF-type composites, the average size of the embedded MNPs is highly dependent on pore dimensions in MOFs, and due to that the pores can act as a scaffold to direct the in situ growth of MNPs.<sup>[38]</sup> In fact, the integration of MOFs and MNPs into a single nanostructure will create synergetic effects, and the multifunctional catalysts are capable of catalyzing cascade reactions. For example, core–shell structured Pd@IRMOF-3 were highly efficient in a cascade reaction, where IRMOF-3 was used as the alkaline catalysts for Knoevenagel condensation, and Pd cores could catalyze the selective hydrogenation of the products from the Knoevenagel condensation reaction.<sup>[39]</sup>

As shown in Figure 1e, in brief, our synthetic strategy involves the redispersion of Cu<sub>2</sub>O in ethanol, followed by addition of an 1,4-benzenedicarboxylic acid (H<sub>2</sub>BDC) solution (dissolved in DMF). Cu<sub>2</sub>O nanocubes would gradually release Cu<sup>+</sup> ions which were further oxidized by the dissolved oxygen to construct 2D frameworks. Furthermore, the obtained Cu-BDC nanosheets were

explored as support materials of incorporating various MNPs (e.g., Au, Ag, Pt, and Ru NPs) with the assistance of 3-mercaptopropionic acid (MPA) as molecular linkers. Finally, the workabilities of Cu-BDC/M nanocatalysts were examined in the condensation reactions between benzaldehyde and primary amines.

## 2. Results and Discussion

### 2.1. Synthesis of Cu-BDC Nanosheets and Bulk Cu-BDC

To begin with, Cu<sub>2</sub>O nanocubes with an average edge side of 60 nm were synthesized,<sup>[40]</sup> as shown in Figure 2a. Afterward, by simply mixing the Cu<sub>2</sub>O nanocubes (suspension in ethanol) with an H<sub>2</sub>BDC solution (dissolved in DMF) at room temperature for 4 h, the desired product (i.e., Cu-BDC nanosheets) could be obtained. Such chemical and structural transformations were clearly observed from the color change of the mixture: from yellow to blue (insets in Figure 2). The morphology,

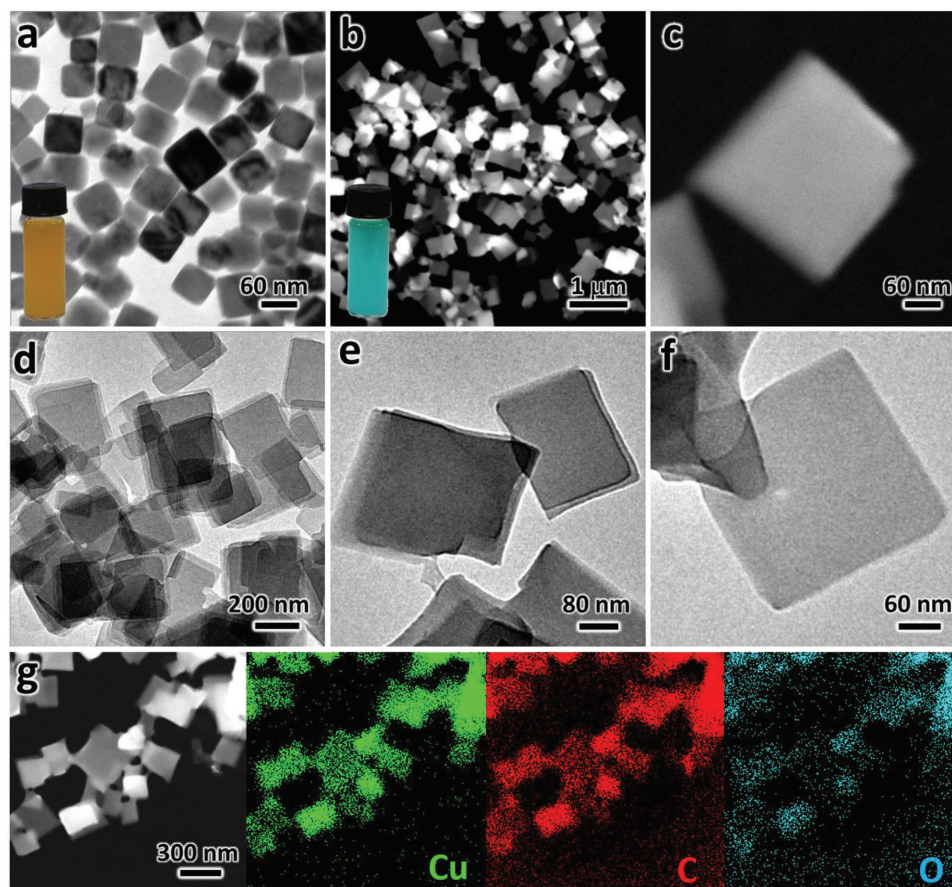


**Figure 2.** a) Representative TEM image of  $\text{Cu}_2\text{O}$  nanocubes; b,c) HAADF-STEM images and d–f) TEM images at different magnifications of the Cu-BDC nanosheets prepared by using  $\text{Cu}_2\text{O}$  as the copper ion source. g) STEM image and the corresponding EDX elemental maps of the Cu-BDC nanosheets. Insets in (a) and (b) are the photographs of  $\text{Cu}_2\text{O}$  nanocubes and Cu-BDC nanosheets ethanolic suspensions, respectively.

structure, porosity, and composition of the as-prepared Cu-BDC nanosheets were fully characterized by various techniques. First, the high-angle annular dark-field scanning transmission electron microscopy (HAADF-STEM; Figure 2b,c) and transmission electron microscopy (TEM; Figure 2d–f) images clearly show that the product consists of very thin lamellae with square morphology and a mean edge length of  $\approx 300$  nm. The high-resolution TEM of the Cu-BDC nanosheets cannot be clearly recognized, likely due to that MOFs are unstable under the exposure of the energetic electron beam.<sup>[39]</sup> Energy-dispersive X-ray (EDX) elemental maps show that the elements C, O, and Cu are distributed uniformly throughout the whole sheet (Figure 2g). On the contrary, as shown in Figure S1a,b in the Supporting Information, the conventional solvothermal synthesis with  $\text{Cu}(\text{NO}_3)_2$  as copper ion source yields bulk MOF crystals with edge dimensions of several micrometers (2–10  $\mu\text{m}$ ), which will be mentioned as Cu-BDC bulk materials hereafter. The comparisons between Cu-BDC nanosheets and bulk-type Cu-BDC were further examined by other techniques in the following sections.

Moreover, when using big  $\text{Cu}_2\text{O}$  microparticle (size of 0.4  $\mu\text{m}$ ) as the copper ion source, the obtained Cu-BDC exhibits nanoparticles shape instead of nanosheet shape (see Figure S1c,d, Supporting Information). The results indicate that the supplying manner of copper ion source will greatly affect the shapes

of Cu-BDC. For instance,  $\text{Cu}(\text{NO}_3)_2$  is a well-soluble metal salt which leads to homogeneously distributed nucleation sites of Cu-BDC in the whole solution. In contrast,  $\text{Cu}_2\text{O}$  nanocubes are spatially inhomogeneous copper ion sources across the solution, which can ideally initiate nucleation and subsequent growth of MOF seed crystals within isolated domains. Therefore, the shapes of Cu-BDC products from using  $\text{Cu}_2\text{O}$  as copper ion source are dependent on the oxidative dissolution rate of  $\text{Cu}_2\text{O}$  and the coordination rate of  $\text{Cu}^{2+}$  and  $\text{BDC}^{2-}$ . We believe that the growth mechanism of Cu-BDC nanosheets can be divided into three consecutive steps: (1) gradual release of  $\text{Cu}^+$  ions from  $\text{Cu}_2\text{O}$  nanocubes; (2) oxidation of  $\text{Cu}^+$  to  $\text{Cu}^{2+}$  ions by the dissolved oxygen; and (3) nucleation-growth of Cu-BDC to construct 2D frameworks by coordination between  $\text{Cu}^{2+}$  and  $\text{BDC}^{2-}$ . It is worth noting that the copper ions for constructing Cu-BDC are absolutely provided by  $\text{Cu}_2\text{O}$  nanocubes.

## 2.2. Characterizations of Cu-BDC Nanosheets

X-ray diffraction (XRD) experiments were followed to confirm whether our product is crystallographically pure Cu-BDC. First, as shown in Figure 3a, the experimental pattern of bulk-type MOFs (viz., with copper nitrate as copper ion source) matched

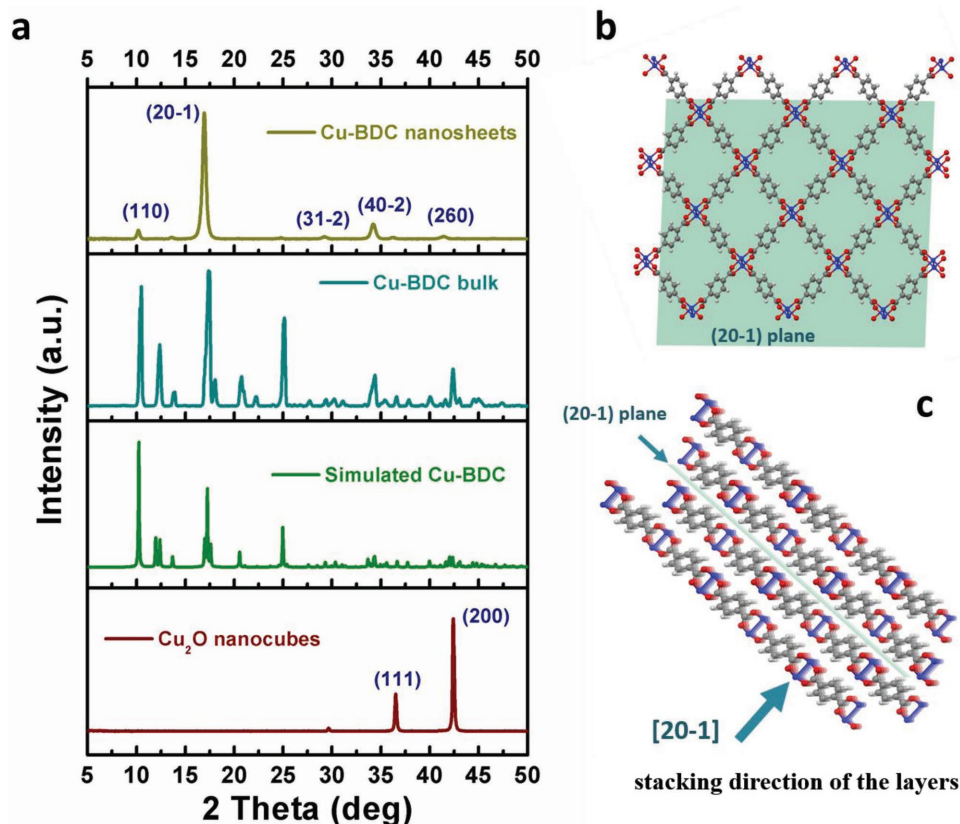


**Figure 3.** a) XRD patterns of  $\text{Cu}_2\text{O}$  nanocubes and Cu-BDC products (nanosheets or bulk materials prepared by using  $\text{Cu}_2\text{O}$  or  $\text{Cu}(\text{NO}_3)_2$  as copper ion sources). The theoretical pattern of Cu-BDC labeled “simulated” is the predicted powder pattern based on the single-crystal structural assignment. b,c) A hypothetical view of the desolvated Cu-BDC structure (i.e., without DMF solvent) on the  $(2\ 0\ -1)$  plane (colored in blue) and the packing diagram along  $[2\ 0\ -1]$  axis illustrating the stacking of lamellar structures that are covalently bonded.

well with the predicted powder diffraction pattern of Cu(BDC) (DMF), in which all the Bragg diffractions were detected, thus revealing that no oriented growth was found in the bulk-type Cu-BDC. In contrast, XRD patterns of the Cu-BDC nanosheets exhibited mainly  $(2\ 0\ -1)$  and  $(4\ 0\ -2)$  crystallographic planes, suggesting that these planes are all perpendicular to the stacking direction of the layers or say that the flat top and bottom surfaces of Cu-BDC nanosheets are bound by  $[2\ 0\ -1]$  facets.<sup>[20]</sup> No XRD peaks belonging to  $\text{Cu}_2\text{O}$  was found in the MOF products, indicating the total conversion of  $\text{Cu}_2\text{O}$  to Cu-BDC. As depicted in Figure 3b,c, the MOF structure extends on the  $(2\ 0\ -1)$  crystallographic plane with identical Cu dimer units linked to  $\text{BDC}^{2-}$  linkers to yield 2D layers.<sup>[16,41]</sup> These sheets are then connected through weak stacking interactions between the adjacent layers (e.g., hydrogen-bonding). On the basis of the above results, it can be concluded that the usage of  $\text{Cu}_2\text{O}$  as copper ion source plays an important role in the construction of Cu-BDC nanosheets with oriented growth.

Fourier-transform infrared spectroscopy (FTIR) spectra of Cu-BDC nanosheets are displayed in Figure 4a, in which the characteristic bands are associated with the organic ligands, DMF solvent, and the copper coordination groups in the frameworks. For instance, the observed bands at 1578, 1501, 1399, 1156, and 1017  $\text{cm}^{-1}$  are all associated with benzene rings of  $\text{H}_2\text{BDC}$  ligand.<sup>[42]</sup> And the  $-\text{COO}-$  group is characterized by the two

bands at 1624 and 1439  $\text{cm}^{-1}$  belonging to the antisymmetric and symmetric stretch modes, respectively. The splitting  $\Delta$  between the two  $\nu(\text{COO})$  frequencies is 185  $\text{cm}^{-1}$ , indicating a bidentate configuration of the carboxylate ligand.<sup>[43]</sup> The  $\text{C}-\text{O}-\text{Cu}$  stretching exhibits the characteristic band at 1110  $\text{cm}^{-1}$ .<sup>[44]</sup> The band at 1666  $\text{cm}^{-1}$  is assigned to the carbonyl group in DMF.<sup>[22]</sup> Other observed bands are attributed to the moisture or the  $\text{C}-\text{H}$  characters (mainly in the fingerprint region). The atomic force microscopy (AFM) image ( $2\ \mu\text{m} \times 2\ \mu\text{m}$ ) in Figure 4b shows several Cu-BDC nanosheets with thickness below 6 nm. Considering that Cu-BDC nanosheets are oriented along  $[2\ 0\ -1]$  and the inter-layer distance between  $(2\ 0\ -1)$  planes is about 5.2 Å, the stacking layers in the thin nanosheets should be less than 10 layers. The thermal stability of Cu-BDC nanosheets was studied by using thermogravimetric analysis (TGA). As shown in Figure 4c, the TGA profile taken in the air (or nitrogen) of Cu-BDC nanosheets suggests the MOF structures are stable up to 300 °C. The coordinated DMF molecule was liberated by heating to 150 °C, where the weight loss accounting of 24 wt% corresponds well to the loss of one DMF molecule per monomer. And the weight loss occurred in the temperature range of 300 and 330 °C is due to the decomposition of  $\text{BDC}^{2-}$  linkers from the MOFs. The evolved gases during the TGA experiments include water,  $\text{CO}_2$ , and  $\text{NO}_2$ , as illustrated by the TGA coupled with FTIR characterization in Figure 4d. The weight calculation indicates that the mole ratio

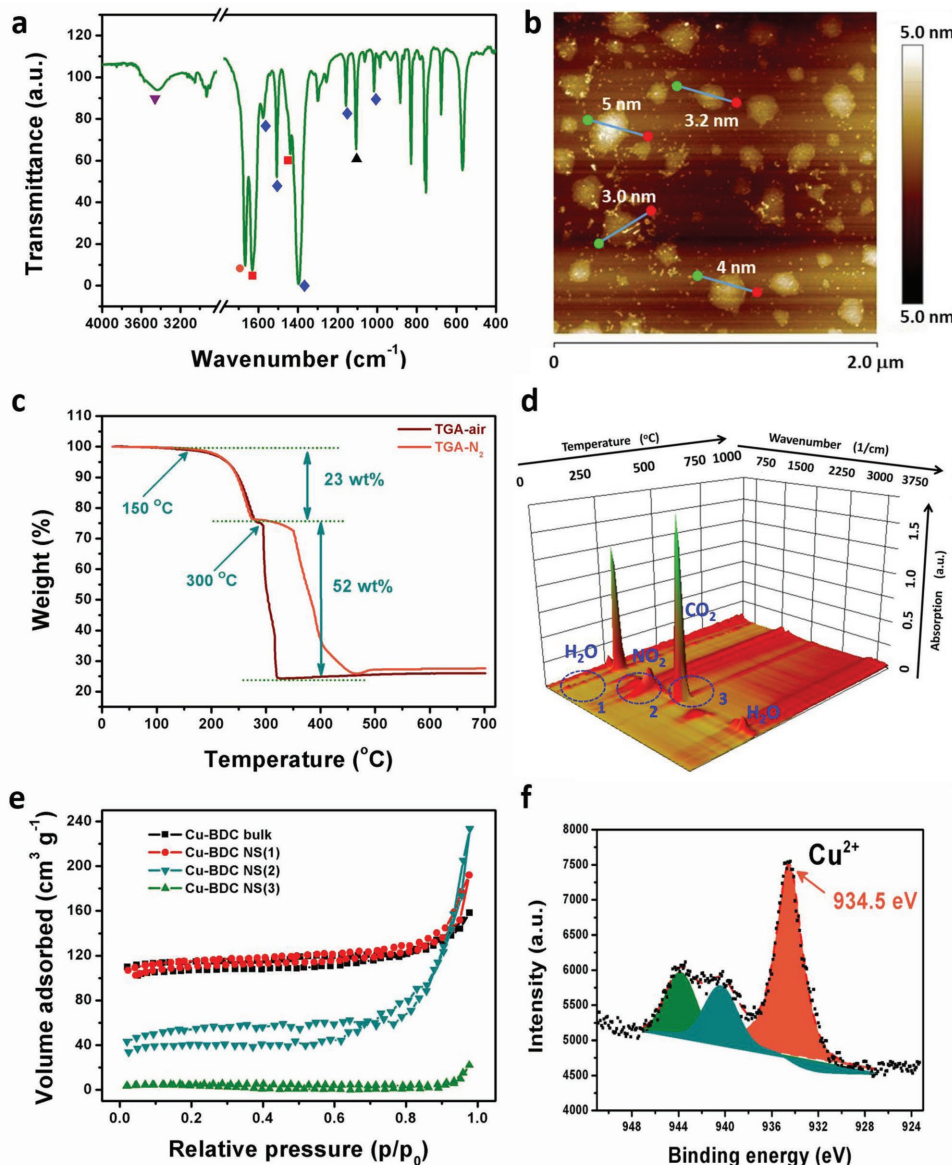


**Figure 4.** Characterizations of Cu-BDC nanosheets. a) FTIR spectrum of Cu-BDC nanosheets, in which the symbols represent the specific organic groups discussed in the main text. b) 2D height AFM image ( $2\ \mu\text{m} \times 2\ \mu\text{m}$ ) of several Cu-BDC nanosheets (where the thickness data were acquired by measuring the height profiles along the tracks shown in the micrograph). The white spots in the AFM image indicate corrugated layers of small nanosheets. c) TGA profiles of Cu-BDC nanosheets in air and  $\text{N}_2$ . d) 3D-FTIR spectra of the evolved gases from TGA analysis using air. e)  $\text{N}_2$  sorption isotherms at 77 K of Cu-BDC nanosheets and Cu-BDC bulk material under different activation conditions, in which NS(3), NS(2), and NS(1) represent Cu-BDC nanosheets activated at 120, 200, and 250 °C for 12 h prior to the tests, respectively. f) XPS core-level spectrum of Cu  $2p_{3/2}$  in Cu-BDC nanosheets sample.

of  $\text{Cu}^{2+}$ :BDC ligand:DMF is around 1:1:1, with an empirical formula of  $[\text{Cu}(\text{BDC})(\text{DMF})]$ . This result is similar to the TGA results of Cu-BDC bulk materials (Figure S2, Supporting Information), indicating that both MOFs share the same composition.

The porosity of the desolvated Cu-BDC nanosheets and bulk-type Cu-BDC was measured by  $\text{N}_2$  sorption-desorption isotherms at 77 K, as displayed in Figure 4e. The Cu-BDC nanosheets exhibit Brunauer-Emmett-Teller (BET) and Langmuir specific surface areas of 372 and 491  $\text{m}^2\ \text{g}^{-1}$ , respectively, both of which are slightly higher than those values from Cu-BDC bulk materials (372 vs 318, and 491 vs 471). And

the micropore volume and micropore area in the Cu-BDC nanosheets were calculated as 0.136  $\text{mL}\ \text{g}^{-1}$  and 293  $\text{m}^2\ \text{g}^{-1}$  from the corresponding t-plot analysis. Moreover, we found that an activation treatment was necessary to reach the maximal surface area and pore volume which indicates that the evolution of porosity proceeds upon heat treatments by removing the DMF guest molecules. As shown in Table S1 in the Supporting Information, the BET surface area gave the following values: 16, 117, and 372  $\text{m}^2\ \text{g}^{-1}$  for the Cu-BDC nanosheets activated at 120, 200, and 250 °C for 12 h prior to the tests, respectively. Therefore, it was believed that the pores in the MOFs can only be detected by

$N_2$  upon thermal desolvation of Cu-BDC to eliminate the DMF solvents.<sup>[16]</sup> As shown in Figure 4f, for Cu-BDC nanosheets sample, the characteristic XPS peak of Cu  $2p_{3/2}$  was observed at a binding energy (BE) of 934.5 eV, together with the presence of two well-known “shake-up satellites,” suggesting the distribution of all divalent Cu(II) species in MOFs. The result also indicates that the copper ions from  $Cu_2O$  precursor were oxidized to  $Cu^{2+}$  before the coordination with organic linkers (i.e.,  $BDC^{2-}$ ).

### 2.3. Fabrication of Cu-BDC/M Integrated Nanocomposites

To demonstrate the structural advantages of Cu-BDC nanosheets as support materials for heterogeneous catalysts, we separately deposit Au, Ag, Pt, and Ru NPs onto the MOF nanosheets. First, we started with introducing Au NPs onto the Cu-BDC nanosheets, that is, the MOFs nanosheets were mixed with a gold precursor (e.g., aqueous  $HAuCl_4$ ), followed

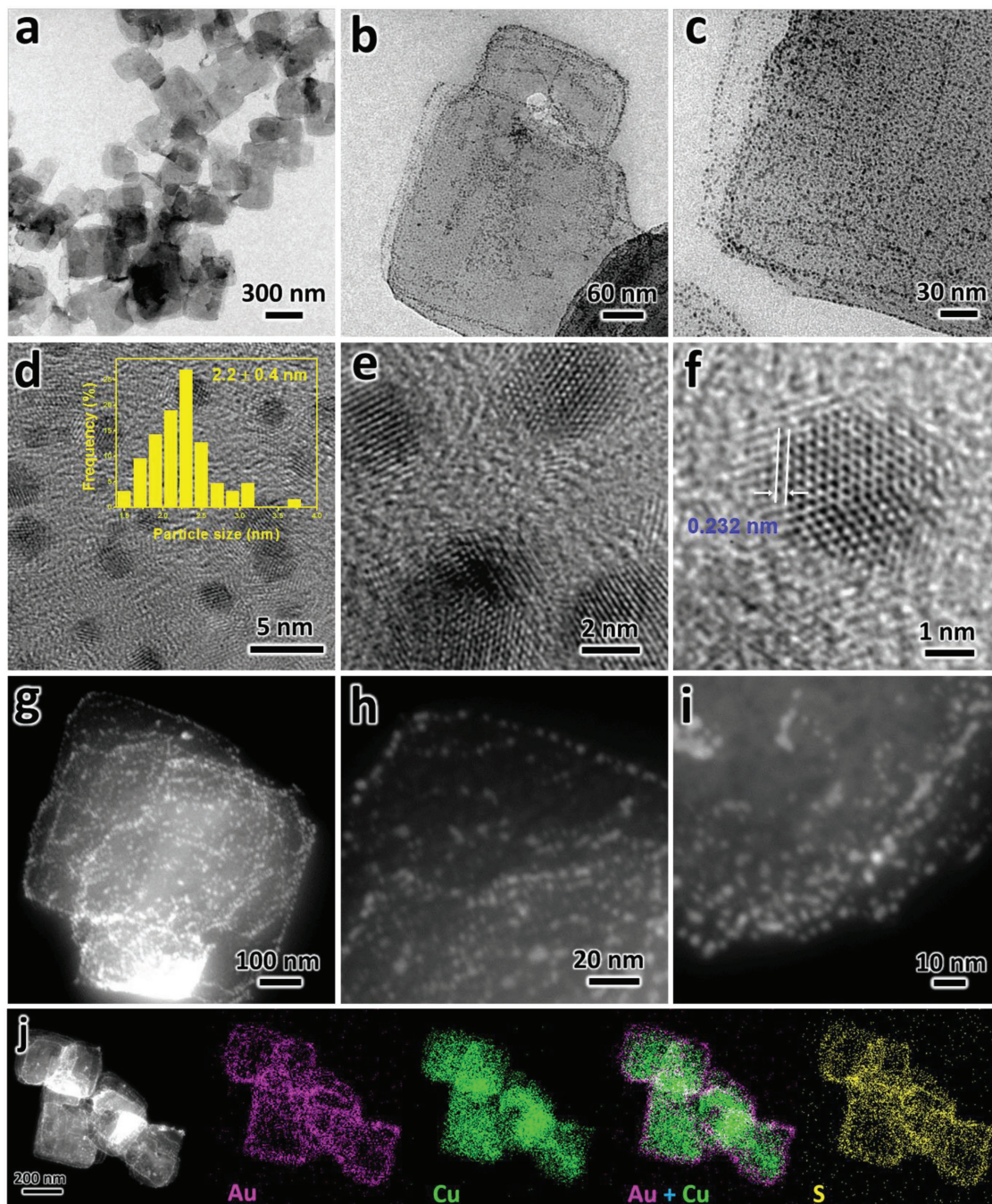


**Figure 5.** Characterization of Cu-BDC/Au catalysts. a–c) TEM images, d–f) HRTEM images, g–i) HAADF-STEM images, and j) the corresponding EDX elemental maps of Cu-BDC/Au nanocatalysts. Inset in (d) shows the corresponding size distribution of gold nanoparticles. Refer to the corresponding EDX pattern and more TEM images in Figures S4–S7 in the Supporting Information.

by a reductive conversion of  $\text{Au}^{3+}$  to Au NPs by the reductants (e.g., R-NBH<sub>4</sub>). In order to enhance the interaction between Au NPs and the MOFs, MPA was used which contained a carboxyl group on one end and a thiol group on the other end (see Figure S3, Supporting Information). During the synthesis, the carboxylate anion on MPA could chelate with the coordinatively unsaturated  $\text{Cu}^{2+}$  on the exterior surface of MOFs nanosheets; meanwhile, the thiol group could bind to the Au NPs. After the immobilization of Au NPs onto Cu-BDC nanosheets, the morphology of Cu-BDC nanosheets could be maintained, and Au NPs were uniformly dispersed, as confirmed by TEM, high-resolution TEM (HRTEM), HAADF-STEM, and EDX elemental mapping images (Figure 5). The thiolate-protected MNPs were very small with an average size of 2.2 nm which were distributed on the external surface of the MOF nanosheets. Since the nanosheets are very thin, the loading positions of the NPs are derived from mostly external surface. This is one of the reasons why abundant NPs were observed in the edges of nanosheets under the TEM and STEM observations. However, as the surface free energies of lower coordinated cations at edges are higher than that of cations on the bottom or top face on

nanosheets,<sup>[45]</sup> NPs are easier to be deposited on the edge of the nanosheet rather than on the faces. The *d* space of the lattice measured at 0.232 nm in Figure 5f gives evidence for Au (111) planes. The existence of S signal from the EDX elemental maps also verifies the molecular binder role of MPA (see Figure 5j). Furthermore, we found the amount of gold loading on the Cu-BDC support was highly dependent on the amount of MPA, even using the same amount of HAuCl<sub>4</sub> precursors. For instance, the gold loadings on Cu-BDC/Au catalysts were 5.5, 7.9, and 9.1 wt%, by adding 0, 0.15, and 0.3 mL MPA (0.1 M) during the synthesis, respectively (under any other identical condition), which represents a higher metal efficiency when using MPA as a molecular linker.

Likewise, other catalytic metal species were introduced on Cu-BDC nanosheets in a similar manner. As illustrated in Figures 6–8, Pt NPs, Ru NPs, and Ag NPs were separately deposited on the exterior surface of Cu-BDC nanosheets. As expected, by the assistance of MPA, the sizes of these MNPs are quite small, which is highly desirable for heterogeneous catalysis. As shown, the average sizes of Pt NPs, Ru NPs, and Ag NPs were 2.5, 3.1, and 4.3 nm, respectively. Moreover,

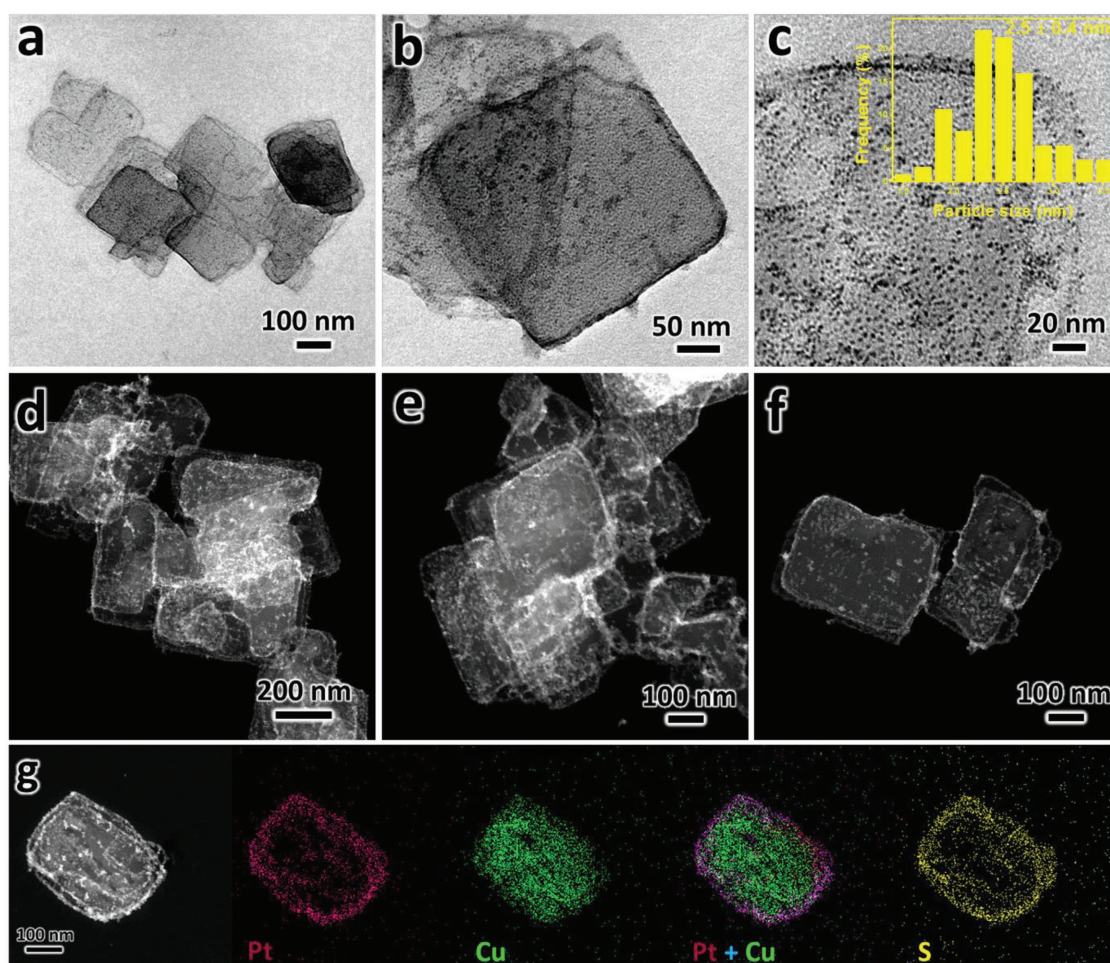


**Figure 6.** Characterizations of Cu-BDC/Pt catalysts. a–c) TEM images, d–f) HAADF-STEM images, and g) the corresponding EDX elemental maps of Cu-BDC/Pt nanocatalysts. Inset in (c) shows the corresponding size distribution of Pt NPs. Referring the corresponding EDX pattern in Figure S8 in the Supporting Information.

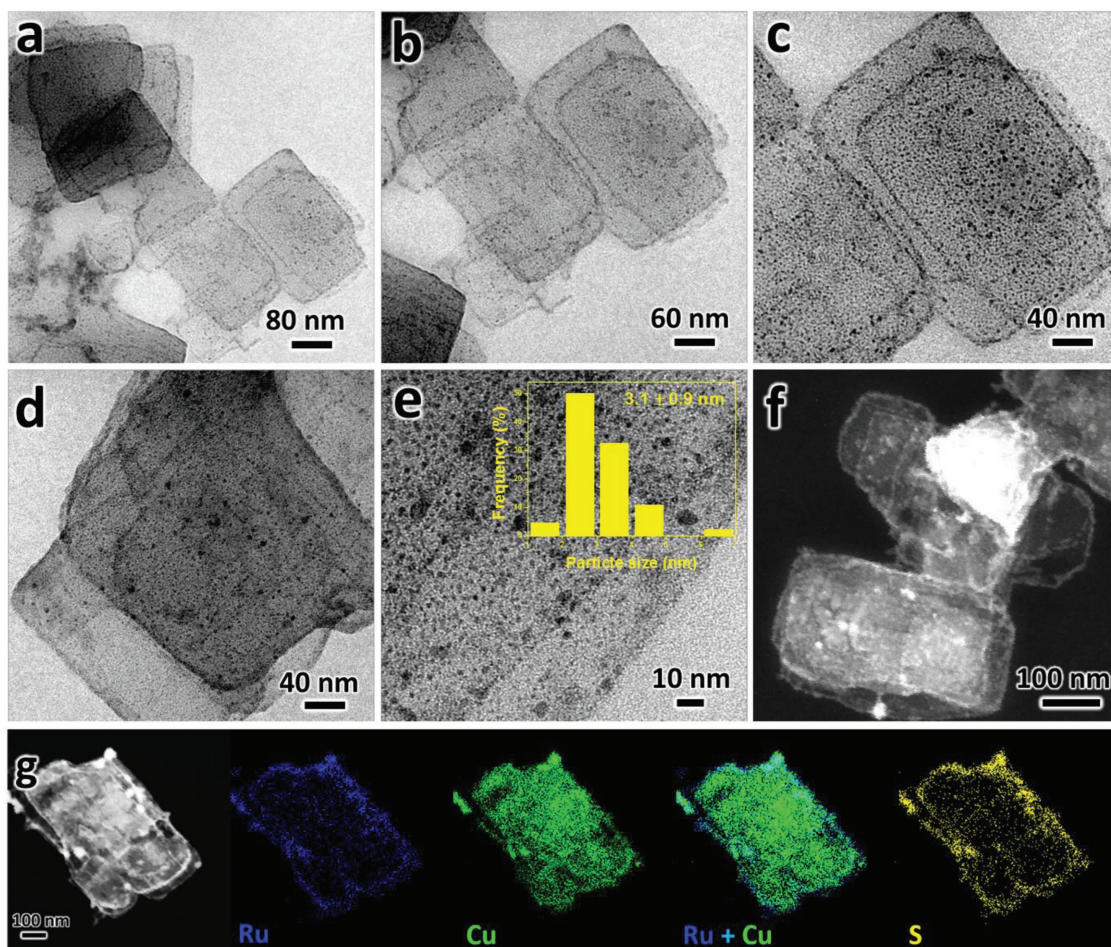


**Figure 7.** Characterization of Cu-BDC/Ru catalysts. a–e) TEM images, f) HAADF-STEM image, and g) the corresponding EDX elemental maps of Cu-BDC/Ru nanocatalysts. Inset in (e) shows the corresponding size distribution of Ru NPs. Refer to the corresponding EDX pattern in Figure S9 in the Supporting Information.

XPS characterizations also confirm the successful preparation of supported metal catalysts (Figure 9). All of the XPS results reveal the formation of MNPs in the zerovalent state (metallic state).<sup>[46–49]</sup> It was found that these values are slightly higher than those of bulk metals, probably due to the metal-to-sulfur charge transfer as the result of thiol–metal bonds at the surface of the thiol-capped NPs.<sup>[46–49]</sup> Figure 9e shows the XPS spectra of the Cu-BDC/Au in S 2*p* regions. The fitting results indicate that S 2*p*<sub>3/2</sub> and S 2*p*<sub>1/2</sub> peaks centering at BEs of 162.6 and 163.8 eV, respectively, are mainly characterized to S–M (M = metals: Au, Pt, Ag, or Ru).<sup>[46]</sup> Moreover, the characteristic XRD peaks due to MNPs in the MOFs/M hybrid are indistinguishable, indicating the formation of very small MNPs.<sup>[39]</sup> In addition, the formation of MNPs was accompanied by a partial degradation of MOF structure as the reductant tetrabutylammonium borohydride (R-NBH<sub>4</sub>) would lead to the partial reduction of copper ions in the MOFs (see Figure 9f). This is also the reason why the characteristic XRD peaks due to MOFs shift towards lower angles after the loading of MNPs (shown in Figure S11a, Supporting Information), suggesting an expansion of the cell volume due to the partial reduction of the copper ions. We also try to use other conventional reductants (such as NaBH<sub>4</sub> and

H<sub>2</sub> (at 250 °C)) to prepare Cu-BDC/M composite. XPS spectra of the two comparison samples together with the sample prepared by using R-NBH<sub>4</sub> reductant are shown Figure S11b,c in the Supporting Information. Similarly, the copper ions in the MOFs were partially reduced when using NaBH<sub>4</sub> as reductant, and most of the copper ions were reduced when using H<sub>2</sub> at high-temperature heating. This is due to the standard reduction potential of the gold precursor (AuCl<sub>4</sub><sup>–</sup> + 3e<sup>–</sup> → Au + 4Cl<sup>–</sup>) that is about 1.00 V (vs standard hydrogen electrode), while the standard reduction potential of Cu<sup>2+</sup> in MOFs is about 0.34 V.<sup>[50]</sup> The calculated amounts of Cu<sup>0</sup> in the composites from the XPS analysis were 17%, 55%, and 78%, respectively, by using R-NBH<sub>4</sub>, NaBH<sub>4</sub>, and H<sub>2</sub> (at 250 °C) as reductants. Therefore, it was found that R-NBH<sub>4</sub> is a relatively mild reductant as compared with other conventional reductants.

#### 2.4. Catalytic Applications of Cu-BDC/M Nanocomposites

Schiff bases continue to play an important role in organic and biological chemistry,<sup>[51–54]</sup> which can be synthesized from the acid-catalyzed condensation of a primary amine with a carbonyl

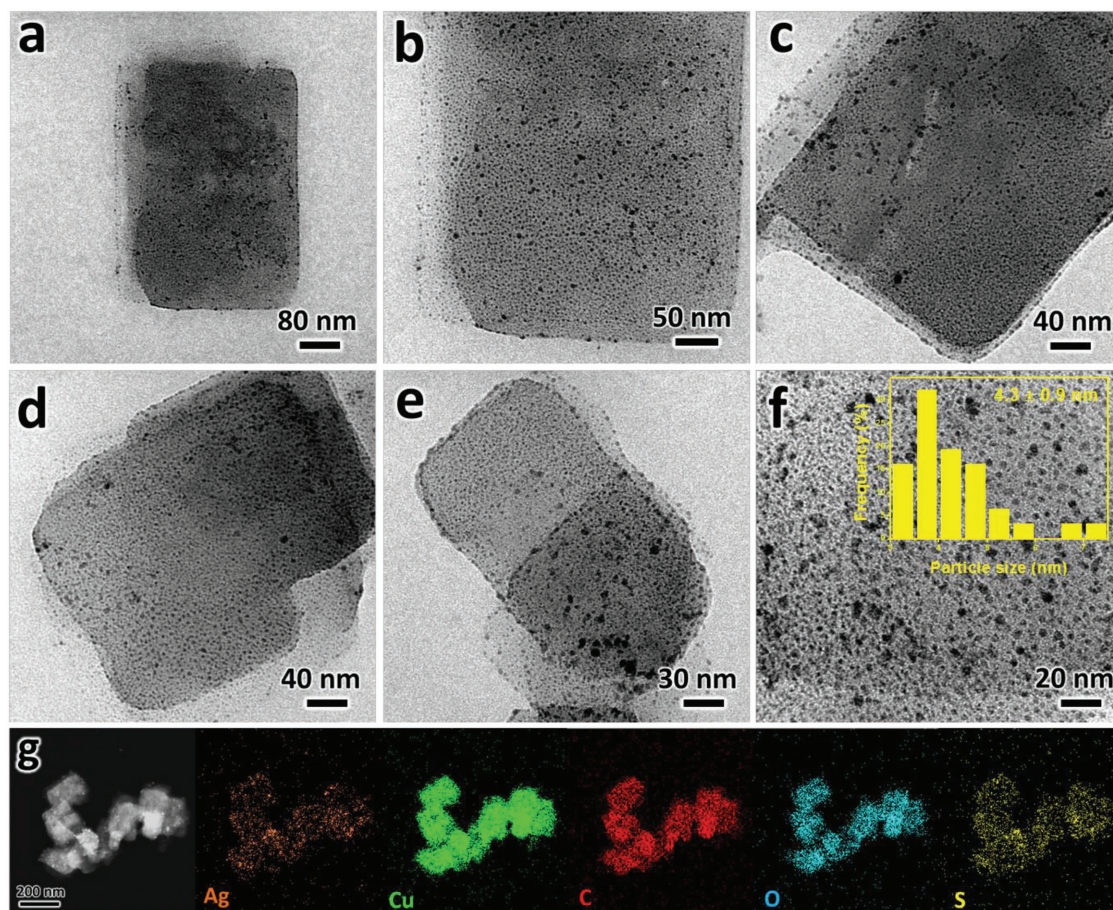


**Figure 8.** Characterization of Cu-BDC/Ag catalysts. a–f) TEM images and g) the corresponding EDX elemental maps of Cu-BDC/Ag nanocatalysts. Inset in (f) shows the corresponding size distribution of Ag NPs. Refer to the corresponding EDX pattern in Figure S10 in the Supporting Information.

compound (e.g., aldehyde). As mentioned before, Cu-BDC contains coordinatively unsaturated metal centers, which are potential as Lewis acid sites in condensation reactions. And the combination of MNPs with Cu-BDC nanosheets is expected to exhibit improved catalytic activity based on synergetic effects from the two components. Therefore, the as-synthesized Cu-BDC and Cu-BDC/Au were used to catalyze the condensation reactions of benzaldehyde with three different primary amines (e.g., ethanolamine, aniline, and 4-aminothiophenol). For comparison, blank experiments without catalysts showed inferior activity under the studied conditions, indicating the importance of Lewis acid sites. When the studied amine was aliphatic amine with short carbon chain (viz., ethanolamine), the reaction rates over both Cu-BDC and Cu-BDC/Au were quite fast. As shown in Tables S2 and S3 in the Supporting Information, the product yielded from the condensation of ethanolamine and benzaldehyde are higher than 96% at a short reaction time of 15 min, for using Cu-BDC or Cu-BDC/Au as catalysts.

It was found that the reaction rate became much slower when two different aromatic amines were tested. The reaction scheme is displayed in **Figure 10a**. Impressively, it was observed that the Cu-BDC/Au greatly increased the reaction rate as compared with pristine Cu-BDC nanosheets as catalysts, especially in the initial stage of the reaction (reaction time <60 min; see

Figure 10b,c and the corresponding GC spectra in Figures S12 and 13, Supporting Information). This trend is the same for using both aromatic amines (aniline and 4-aminothiophenol) as substrates. However, as 4-aminothiophenol was used instead of aniline, the reaction rate was enhanced a lot. The result suggests that the electron-donating para substituents (–SH) on aniline would increase the reaction rate, which is consistent with a previous report.<sup>[55]</sup> When the reduced Cu-BDC sample prepared by heating in H<sub>2</sub> at 250 °C (Cu<sup>2+</sup> → Cu<sup>0</sup>) was utilized as a catalyst (Figure S11b, Supporting Information), it exhibited very low conversion of benzaldehyde (21%), suggesting that partially coordinated Cu<sup>2+</sup> sites are critical for the catalytic reaction. This phenomenon is similar to the study by Mobinikhaledi et al. who used Cu(II) salt<sup>[56]</sup> as a homogeneous catalyst for Schiff bases synthesis. The effect of gold loading amount on the catalytic performance can be found in Figure 10d. Obviously, a higher gold loading led to a higher yield of imine product, which further confirms that synergetic effects were raised by the integration of 2D MOF support and Au NPs. Similarly, the loading of Au nanoparticles on reduced Cu-BDC also enhanced the catalytic performance. And it is believed that thiol group (from the MPA) only exists in the space between Cu-BDC flat surface and gold nanoparticles, which is similar to layer-by-layer assembly method to deposit Au NPs on a flat substrate functionalized

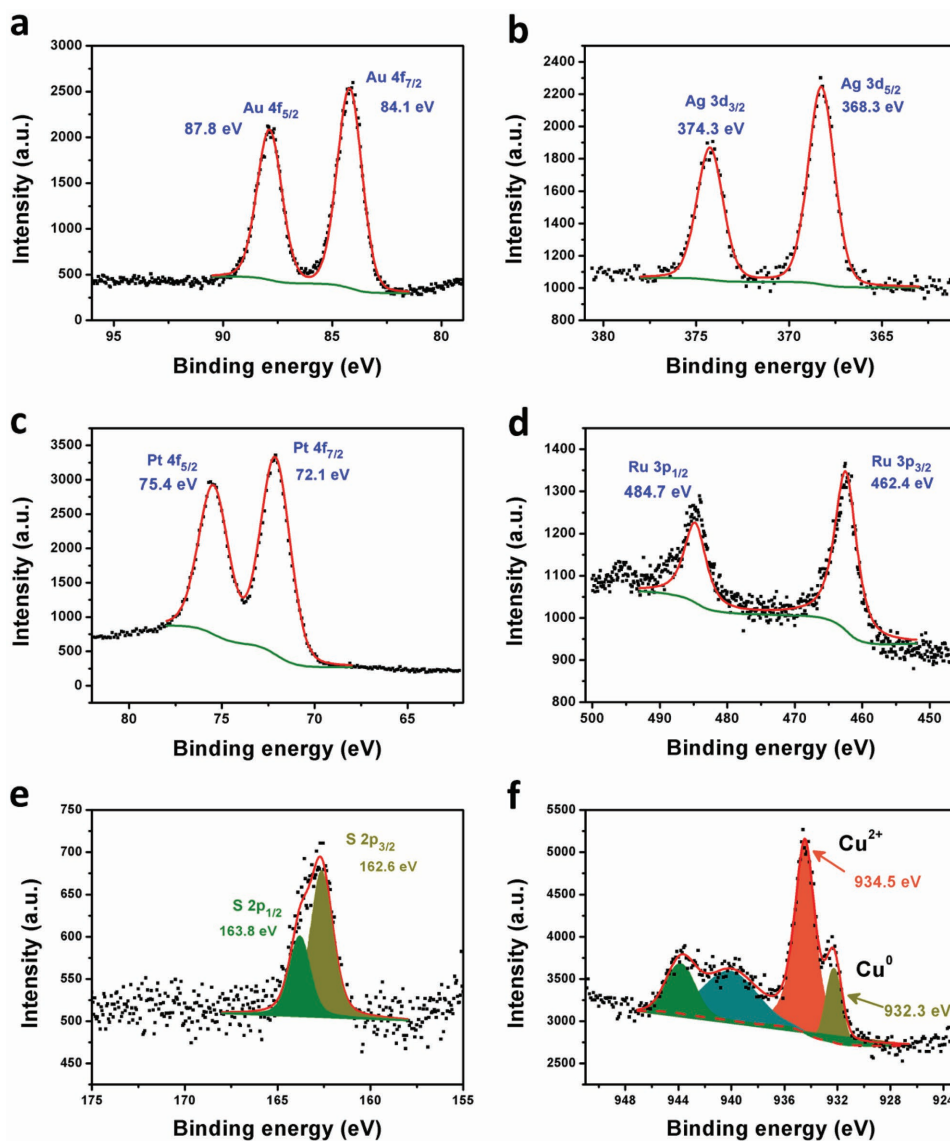


**Figure 9.** XPS spectra of Cu-BDC/M nanocatalysts for the identification of the metal chemical states. a) Au 4f, b) Ag 3d, c) Pt 4f, d) Ru 3p, e) S 2p, and f) Cu 2p<sub>3/2</sub> XPS core-level spectra of in the Cu-BDC/M nanocatalyst samples. M = Au in (a,e,f), M = Ag in (b), M = Pt in (c), and M = Ru in (d).

with thiol group.<sup>[57]</sup> Moreover, Figure S14 in the Supporting Information shows the catalytic performance of the other three catalysts (viz., Cu-BDC/Ag, Cu-BDC/Pt, and Cu-BDC/Ru) for condensation reactions between benzaldehyde and aniline. It was found that loading of Au NPs on Cu-BDC nanosheets exhibited superior catalytic performance than loading other NPs on Cu-BDC.

We also compare the catalytic activities of Cu-BDC nanosheets and Cu-BDC bulk material in condensation of benzaldehyde with aniline in toluene. The equilibrium conversion of benzaldehyde was 70% and 50%, respectively, for Cu-BDC nanosheets and Cu-BDC bulk material, indicating that the nanosheet structure of Cu-BDC benefits the formation of more accessible active sites on the external surface (i.e., partially coordinated Cu<sup>2+</sup> and Au NPs) and the reaction species

over bulk Cu-BDC involve longer molecular diffusion distance. The recyclability of the catalysts has also been checked for both condensation reactions between benzaldehyde and aromatic amines. As shown in Figure 10e, the designed Cu-BDC/Au can be repeatedly used for at least five consecutive reaction cycles with only slight activity loss. And the slight activity loss was caused by (i) slight decrease of Au loading in the spent catalysts (i.e., 8.9 and 8.5 wt% in the two cases), where 9.1 wt% of Au loading was present in the fresh catalyst, and (ii) the loss of solid catalyst during the repeated experiments. The condensation reactions studied in our work are only simple demonstrations for examining the workability of our designed catalysts, and we believed that the obtained Cu-BDC/Au can also serve as catalysts for other types of acid-catalyzed reactions reported in the literature, such as Knoevenagel condensation reaction,

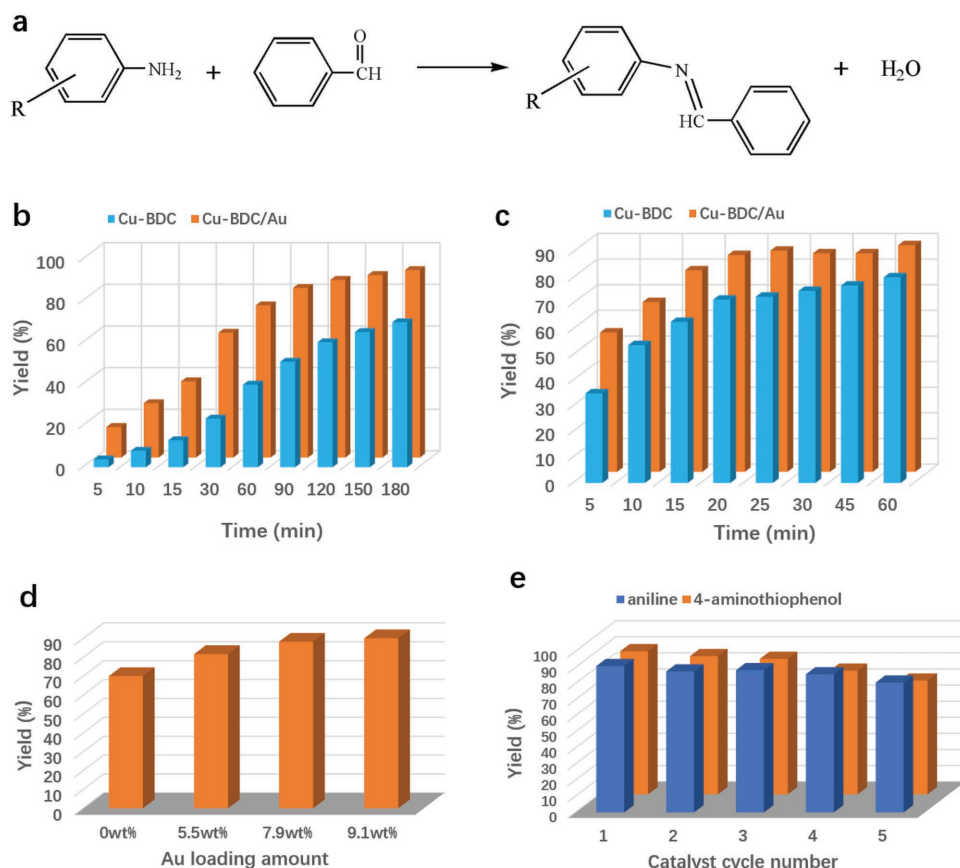


**Figure 10.** a) Condensation reactions between benzaldehyde and aromatic amines, in which R = H for aniline and R = SH for 4-aminothiophenol. b,c) Results of experiments with condensation between benzaldehyde and b) aniline and c) 4-aminothiophenol over pristine Cu-BDC and Cu-BDC/Au catalysts, respectively. In the sample of Cu-BDC/Au, gold loading amount was determined as 9.1 wt% by ICP-OES. d) The effect of Au loading amount on the product yield from condensation between benzaldehyde and aniline. And e) catalytic performance of recycling Cu-BDC/Au catalysts in condensation reactions between benzaldehyde and aromatic amines (aniline or 4-aminothiophenol).

C–H arylation reaction, hydroxylation and nitration of aryl halides, cycloaddition of benzyl azide and phenylacetylene, three-component coupling (amines, aldehydes, and alkynes to form the corresponding propargylamines), etc.<sup>[58]</sup>

### 3. Conclusion

In summary, we have demonstrated that 2D Cu-BDC nanosheets can be synthesized by using Cu<sub>2</sub>O nanocubes as copper ion source at mild conditions (i.e., room temperature, atmosphere pressure, and short reaction time), which is very different from the conventional top-down or bottom-up synthetic strategies. The as-prepared 2D Cu-BDC nanosheets with oriented growth are desirable host materials for constructing integrated catalysts. For instance, Au, Pt, Ag, and Ru NPs with uniform size (<5 nm) can be specifically deposited on the exterior surface of Cu-BDC nanosheets with the assistance of MPA as a molecular linker. Furthermore, the obtained Cu-BDC/Au nanocatalysts exhibited excellent catalytic activity in Schiff bases synthesis reactions, and it was believed that synergistic effects between Cu-BDC and Au NPs raised during the catalytic reactions.

### 4. Experimental Section

**Chemicals and Materials:** The following chemicals were used as received without further purification: copper (II) nitrate trihydrate (Merck, 99.5%), copper (II) chloride dihydrate (Aldrich, 99%), H<sub>2</sub>BDC (Aldrich, 98%), gold (III) chloride trihydrate (Sigma-Aldrich, 99.9%), potassium tetrachloroplatinate (II) (Sigma-Aldrich, 98%), silver nitrate (Merck, 99.0%), ruthenium (III) chloride hydrate (Aldrich, 99%), MPA (Lancaster, 99%), tetrabutylammonium borohydride (R-NBH<sub>4</sub>, 98%, Sigma-Aldrich), polyvinylpyrrolidone (PVP; Fluka, K-30), L-ascorbic acid (Aldrich, 99%), sodium hydroxide (Merck, 99%), aniline (Alfa Aesar, 99%), benzaldehyde (Sigma-Aldrich, 99%), 2-aminoethanol (Sigma-Aldrich, 99%), 4-aminothiophenol (Sigma-Aldrich, 97%), *n*-dodecane (Alfa Aesar, 99%), toluene (J.T. Baker, 99.5%), *N,N'*-DMF (Merck, 99.8%), methanol (Fisher, 99.99%), and ethanol (Fisher, 99.99%). Deionized water was used for all experiments.

**Synthesis of Cu<sub>2</sub>O Nanocubes:** Specifically, 0.1 mmol of CuCl<sub>2</sub> and 0.1 g of PVP were dissolved in 40 mL of water, followed by a dropwise addition (30 μL s<sup>-1</sup>) of 2.5 mL of NaOH (0.2 M). Then, the solution was stirred magnetically for 5 min, followed by a dropwise addition (10 μL s<sup>-1</sup>) of 2.5 mL of ascorbic acid (0.1 M). After the addition, the mixture was further stirred for another 5 min. The product was recovered by centrifugation and then washed with ethanol twice. Finally, the yellow-colored Cu<sub>2</sub>O nanocubes were redispersed into 10 mL of ethanol for the future use.

**Synthesis of Cu-BDC Nanosheets:** 0.5 mmol of H<sub>2</sub>BDC was fully dissolved into 5 mL of ethanol and 5 mL of DMF. To this solution, 10 mL of the above prepared Cu<sub>2</sub>O suspension (in ethanol) was added. The

formation of Cu-BDC nanosheets was carried out at room temperature for 4 h, wherein Cu<sub>2</sub>O nanocubes gradually released Cu<sup>+</sup> ions which were further oxidized by the dissolved O<sub>2</sub> to construct 2D frameworks. Finally, the blue-colored products were collected via centrifugation, followed by washing with methanol, and finally the solid was redispersed in 40 mL of methanol for the future use.

**Synthesis of Cu-BDC Bulk Materials:** Bulk-type Cu-BDC was prepared by using Cu(NO<sub>3</sub>)<sub>2</sub> as copper ion source according to a previously reported method.<sup>[22]</sup> Specifically, equimolar quantities of copper nitrate (7.5 mmol) and H<sub>2</sub>BDC (7.5 mmol) were dissolved in 150 mL of DMF. Then, this solution was solvothermally treated at 110 °C for 36 h. After the reaction, the products were collected via centrifugation, followed by washing with ethanol/DMF twice, drying at 60 °C overnight.

**Synthesis of Cu-BDC/Au-Supported Nanocatalysts:** For a general synthesis, 1 mL of HAuCl<sub>4</sub>·3H<sub>2</sub>O methanolic solution (0.010 M) was mixed with 40 mL of the above-prepared Cu-BDC methanolic suspension. The mixture was stirred for 40 min at room temperature, followed by an addition of 0.3 mL of MPA methanolic solution (0.1 M). After stirring for 5 min, 0.3 mL of R-NBH<sub>4</sub> methanolic solution (0.25 M) was injected into the above mixture. (Note that R-NBH<sub>4</sub> solution was used around 8 min just after the preparation.) The mixture was stirred for 30 s, followed by centrifuging and washing with ethanol twice. Other MNPs (M = Pt, Ag, and Ru) loading on Cu-BDC nanosheets were synthesized in a similar way but changing the corresponding metal precursors and the amount of MPA and R-NBH<sub>4</sub>. Complete descriptions of the synthetic parameters can be found in the Supporting Information.

**Evaluation of Catalytic Activities:** In a typical experiment, 30 mg of catalysts was first dispersed into 10 mL of toluene solvent by sonication, then a mixture containing 1 mmol of benzaldehyde, 1 mmol of aniline (or 4-aminothiophenol, or ethanolamine), and 0.1 mL of *n*-dodecane as an internal standard was added to this catalyst suspension. The reaction mixture was stirred at 80 °C. The reaction rate was monitored by withdrawing aliquots from the reaction mixture at different time intervals, and the liquid after removing catalysts was immediately analyzed by gas chromatography (GC) and GC–mass spectrometry (GC–MS).

**Characterization Techniques:** Morphologies of samples were characterized by field-emission scanning electron microscopy (FESEM; JSM-6700F), TEM (JEM-2010), HAADF-STEM (JEM-2100F), and AFM (Bruker Dimension Icon). The crystallographic information was analyzed by XRD (Bruker D8 Advance) equipped with a Cu K<sub>α</sub> radiation source (λ = 1.5406 Å). The elemental mapping was done by EDX (Model 7426; Oxford Instruments). The surface composition and oxidation state of the samples were further analyzed by X-ray photoelectron spectroscopy (XPS; AXIS-HSi; Kratos Analytical). All binding energies were referred to the C 1s peak (284.5 eV) arising from the C–C bonds. Specific surface areas, pore volume, and pore size of the samples were determined using N<sub>2</sub> physisorption isotherms at 77 K (Quantachrome NOVA-3000 system). TGA studies were carried out on a thermobalance (TGA-2050; TA Instruments) under flowing air (or N<sub>2</sub>) atmosphere (flow rate: 50 mL min<sup>-1</sup>) at a heating rate of 10 °C min<sup>-1</sup>. The organic groups in the MOFs structures were characterized by FTIR (Bio-Rad) by using the potassium bromide (KBr) pellet technique. Gold loading in the catalysts was determined by inductively coupled plasma optical emission spectrometry (ICP-OES; Optima 7300DV; Perkin Elmer, USA).

## Supporting Information

Supporting Information is available from the Wiley Online Library or from the author.

## Acknowledgements

The authors would like to acknowledge National University of Singapore (NUS) for part of the material characterizations and thank Prof. Hua

Chun Zeng for helpful discussions on this project. This work was supported by the Scientific Research Funds of Huaqiao University (No. 18BS102 & 16BS501) and the Program for Innovative Research Team in Science and Technology in Fujian Province University.

## Conflict of Interest

The authors declare no conflict of interest.

## Keywords

2D MOFs, catalysis, metal-organic frameworks, nanosheets, Schiff bases

Received: September 23, 2018

Revised: November 18, 2018

Published online:

- [1] S. L. James, *Chem. Soc. Rev.* **2003**, 32, 276.
- [2] V. Guillermin, D. Kim, J. F. Eubank, R. Luebke, X. Liu, K. Adil, M. S. Lah, M. Eddaoudi, *Chem. Soc. Rev.* **2014**, 43, 6141.
- [3] B. Y. Guan, X. Y. Yu, H. B. Wu, X. W. Lou, *Adv. Mater.* **2017**, 29, 1703614.
- [4] B. Y. Guan, Y. Lu, Y. Wang, M. Wu, X. W. Lou, *Adv. Funct. Mater.* **2018**, 28, 1706738.
- [5] H. Furukawa, K. E. Cordova, M. O'Keeffe, O. M. Yaghi, *Science* **2013**, 341, 1230444.
- [6] G. Majano, J. Pérez-Ramírez, *Adv. Mater.* **2013**, 25, 1052.
- [7] Y. Mao, J. Li, W. Cao, Y. Ying, P. Hu, Y. Liu, L. Sun, H. Wang, C. Jin, X. Peng, *Nat. Commun.* **2014**, 5, 5532.
- [8] H. Gao, Y. Luan, K. Chaikittikul, W. Dong, J. Li, X. Zhang, D. Jia, M. Yang, G. Wang, *ACS Appl. Mater. Interfaces* **2015**, 7, 4667.
- [9] A. U. Czaja, N. Trukhan, U. Muller, *Chem. Soc. Rev.* **2009**, 38, 1284.
- [10] Y. Liu, W. Zhang, S. Li, C. Cui, J. Wu, H. Chen, F. Huo, *Chem. Mater.* **2014**, 26, 1119.
- [11] H. Guo, G. Zhu, I. J. Hewitt, S. Qiu, *J. Am. Chem. Soc.* **2009**, 131, 1646.
- [12] G. Zhan, H. C. Zeng, *Adv. Funct. Mater.* **2016**, 26, 3268.
- [13] R. Yan, Y. Zhao, H. Yang, X.-J. Kang, C. Wang, L.-L. Wen, Z.-D. Lu, *Adv. Funct. Mater.* **2018**, 28, 1802021.
- [14] A. Urtizberea, E. Natividad, P. J. Alonso, M. A. Andrés, I. Gascón, M. Goldmann, O. Roubeau, *Adv. Funct. Mater.* **2018**, 28, 1801695.
- [15] W. Mori, F. Inoue, K. Yoshida, H. Nakayama, S. Takamizawa, M. Kishita, *Chem. Lett.* **1997**, 26, 1219.
- [16] C. G. Carson, K. Hardcastle, J. Schwartz, X. Liu, C. Hoffmann, R. A. Gerhardt, R. Tannenbaum, *Eur. J. Inorg. Chem.* **2009**, 2009, 2338.
- [17] J. Liu, B. Lukose, O. Shekhah, H. K. Arslan, P. Weidler, H. Gliemann, S. Brase, S. Grosjean, A. Godt, X. Feng, K. Mullen, I.-B. Magdau, T. Heine, C. Woll, *Sci. Rep.* **2012**, 2, 921.
- [18] A. Carné-Sánchez, I. Imaz, M. Cano-Sarabia, D. Maspoch, *Nat. Chem.* **2013**, 5, 203.
- [19] X. Wang, Q. Wang, Q. Wang, F. Gao, F. Gao, Y. Yang, H. Guo, *ACS Appl. Mater. Interfaces* **2014**, 6, 11573.
- [20] T. Rodenas, I. Luz, G. Prieto, B. Seoane, H. Miro, A. Corma, F. Kapteijn, F. X. Llabrés i Xamena, J. Gascon, *Nat. Mater.* **2015**, 14, 48.
- [21] A. Corma, H. García, F. X. Llabrés i Xamena, *Chem. Rev.* **2010**, 110, 4606.
- [22] P. Puthiaraj, P. Suresh, K. Pitchumani, *Green Chem.* **2014**, 16, 2865.
- [23] N. T. S. Phan, T. T. Nguyen, K. D. Nguyen, A. X. T. Vo, *Appl. Catal., A* **2013**, 464–465, 128.
- [24] I. Luz, F. X. Llabrés i Xamena, A. Corma, *J. Catal.* **2012**, 285, 285.

- [25] S. J. Singh, S. R. Kale, M. B. Gawande, A. Velhinho, R. V. Jayaram, *Catal. Commun.* **2014**, *44*, 24.
- [26] G. H. Dang, Y. T. H. Vu, Q. A. Dong, D. T. Le, T. Truong, N. T. S. Phan, *Appl. Catal., A* **2015**, *491*, 189.
- [27] G. H. Dang, T. T. Dang, D. T. Le, T. Truong, N. T. S. Phan, *J. Catal.* **2014**, *319*, 258.
- [28] M. B. Gawande, A. Goswami, F.-X. Felpin, T. Asefa, X. Huang, R. Silva, X. Zou, R. Zboril, R. S. Varma, *Chem. Rev.* **2016**, *116*, 3722.
- [29] P. Li, H. C. Zeng, *ACS Appl. Mater. Interfaces* **2016**, *8*, 29551.
- [30] P. Hu, J. V. Morabito, C.-K. Tsung, *ACS Catal.* **2014**, *4*, 4409.
- [31] Z. Li, H. C. Zeng, *Chem. Mater.* **2013**, *25*, 1761.
- [32] Z. Li, H. C. Zeng, *J. Am. Chem. Soc.* **2014**, *136*, 5631.
- [33] D. Esken, S. Turner, O. I. Lebedev, G. Van Tendeloo, R. A. Fischer, *Chem. Mater.* **2010**, *22*, 6393.
- [34] T. Ishida, M. Nagaoka, T. Akita, M. Haruta, *Chem. - Eur. J.* **2008**, *14*, 8456.
- [35] C.-H. Kuo, Y. Tang, L.-Y. Chou, B. T. Sneed, C. N. Brodsky, Z. Zhao, C.-K. Tsung, *J. Am. Chem. Soc.* **2012**, *134*, 14345.
- [36] L. Ning, S. Liao, X. Liu, P. Guo, Z. Zhang, H. Zhang, X. Tong, *J. Catal.* **2018**, *364*, 1.
- [37] Y. Luan, Y. Qi, H. Gao, N. Zheng, G. Wang, *J. Mater. Chem. A* **2014**, *2*, 20588.
- [38] M. Meilikhov, K. Yusenko, D. Esken, S. Turner, G. Van Tendeloo, R. A. Fischer, *Eur. J. Inorg. Chem.* **2010**, *2010*, 3701.
- [39] M. Zhao, K. Deng, L. He, Y. Liu, G. Li, H. Zhao, Z. Tang, *J. Am. Chem. Soc.* **2014**, *136*, 1738.
- [40] G. Zhan, H. C. Zeng, *ACS Appl. Mater. Interfaces* **2017**, *9*, 37210.
- [41] H. Li, M. Eddaoudi, T. L. Groy, O. M. Yaghi, *J. Am. Chem. Soc.* **1998**, *120*, 8571.
- [42] K. Tan, N. Nijem, P. Canepa, Q. Gong, J. Li, T. Thonhauser, Y. J. Chabal, *Chem. Mater.* **2012**, *24*, 3153.
- [43] G. B. Deacon, R. J. Phillips, *Coord. Chem. Rev.* **1980**, *33*, 227.
- [44] N. A. A. Sani, W. J. Lau, A. F. Ismail, *RSC Adv.* **2015**, *5*, 13000.
- [45] X. Zhang, C. Lian, Z. Chen, C. Chen, Y. Li, *Nano Res.* **2018**, *11*, 4142.
- [46] Y. Joseph, I. Besnard, M. Rosenberger, B. Guse, H.-G. Nothofer, J. M. Wessels, U. Wild, A. Knop-Gericke, D. Su, R. Schlögl, A. Yasuda, T. Vossmeier, *J. Phys. Chem. B* **2003**, *107*, 7406.
- [47] S. Y. Kang, K. Kim, *Langmuir* **1998**, *14*, 226.
- [48] W. Tu, K. Takai, K.-i. Fukui, A. Miyazaki, T. Enoki, *J. Phys. Chem. B* **2003**, *107*, 10134.
- [49] N. Chakroune, G. Viau, S. Ammar, L. Poul, D. Veautier, M. M. Chehimi, C. Mangeney, F. Villain, F. Fiévet, *Langmuir* **2005**, *21*, 6788.
- [50] R. Das, P. Pachfule, R. Banerjee, P. Poddar, *Nanoscale* **2012**, *4*, 591.
- [51] H. Naeimi, J. Safari, A. Heidarneshad, *Dyes Pigm.* **2007**, *73*, 251.
- [52] R. Drozdak, B. Allaert, N. Ledoux, I. Dragutan, V. Dragutan, F. Verpoort, *Adv. Synth. Catal.* **2005**, *347*, 1721.
- [53] C. M. da Silva, D. L. da Silva, L. V. Modolo, R. B. Alves, M. A. de Resende, C. V. B. Martins, Â. de Fátima, *J. Adv. Res.* **2011**, *2*, 1.
- [54] M. A. Sprung, *Chem. Rev.* **1940**, *26*, 297.
- [55] E. F. Pratt, M. J. Kamlet, *J. Org. Chem.* **1961**, *26*, 4029.
- [56] A. Mobinikhaledi, P. J. Steel, M. Polson, *Synth. React. Inorg., Met.-Org., Nano-Met. Chem.* **2009**, *39*, 189.
- [57] J. Wu, Y. Qu, Q. Yu, H. Chen, *Mater. Chem. Front.* **2018**, *2*, 2175.
- [58] A. H. Chughtai, N. Ahmad, H. A. Younus, A. Laypkov, F. Verpoort, *Chem. Soc. Rev.* **2015**, *44*, 6804.